Direct Numerical Simulation of a Turbulent Boundary Layer over Acoustic Liners

Shahzad, H.; Hickel, S.; Modesti, D.

DOI
10.2514/6.2023-3887

Publication date
2023

Document Version
Final published version

Published in
AIAA AVIATION 2023 Forum

AIAA AVIATION Forum
12-16 June 2023, San Diego, CA and Online
AIAA AVIATION 2023 Forum

10.2514/6.2023-3887

Direct Numerical Simulation of a Turbulent Boundary Layer over Acoustic Liners

Haris Shahzad, Stefan Hickel and Davide Modesti
Aerodynamics Group, Faculty of Aerospace Engineering, Delft University of Technology,Kluyverweg 2, 2629 HS Delft, The Netherlands

The nacelle of aircraft engines is coated with acoustic liners to reduce engine noise. An undesirable effect of these liners is that they increase aerodynamic drag. We study this drag penalty by performing Direct Numerical Simulations of a turbulent boundary layer over an acoustic liner array at friction Reynolds number, $Re_\tau \approx 850$–2500. We use this simulation to confirm several findings that we recently brought forward using a simpler channel flow setup [1]. We show that acoustic liners lead to high wall-normal velocity fluctuations that can be directly correlated with a modulation of the classical near-wall cycle and to an increase in drag. We also confirm that the acoustic liners act as permeable surface roughness and the non-linear Forchheimer coefficient is the relevant permeability parameter for scaling the drag increase.

I. Nomenclature

c	=	speed of sound
C_f	=	skin-friction coefficient
d	=	orifice diameter
k	=	cavity depth
L_χ	=	domain length in χ direction
M	=	Mach number
N_χ	=	grid points in χ direction
Re	=	Reynolds number
t	=	orifice thickness
u_∞	=	freestream velocity
u_τ	=	friction velocity
x_t	=	smooth-to-rough transition location
δ	=	boundary layer thickness
δ_v	=	viscous length scale
ΔU^+	=	Hama roughness function
λ	=	cavity cross-section length/width
ν	=	kinematic viscosity
ρ	=	density
σ	=	facesheet porosity
τ_{ij}	=	Reynolds stresses
τ_w	=	wall shear stress

II. Introduction

Aircraft engines are the primary source of noise during take-off and landing. In order to reduce noise, engine nacelles are equipped with noise control devices called acoustic liners. Acoustic liners consist of a porous facesheet and a solid backplate with a honeycomb core in between the two. The perforations and honeycomb core resemble Helmholtz resonators. Acoustic liners exhibit a resonance frequency that can be tuned to the dominant frequency of the engine fan for noise reduction. Due to the passive nature of these devices and their efficacy, acoustic liners are widely used and represent the state of the art in engine noise reduction. However, they behave like roughness and tend to increase aircraft drag. The increase in drag was accepted as a necessary compromise as the need to reduce noise emissions took precedence and acoustic liners have primarily been studied and optimised from an acoustic perspective

[2, 3]. An in-depth understanding of how acoustic liners impact engine aerodynamics and how they modulate the turbulent boundary layer is necessary to be able to optimise them both acoustically and aerodynamically.

Acoustic liners present a permeable rough surface to the incoming flow. Permeable surfaces have been studied far less than impermeable canonical rough surfaces, and basic aspects that are well understood for roughness are still debated for porous surfaces. Manes et al. [4] studied permeable surfaces and compared their results to rough surfaces, noting an increase in the added drag for permeable surfaces as compared to the equivalent rough surface. Breugem et al. [5] and Kuwata and Suga [6] noted that permeable surfaces may even lead to a modified log layer and a breakdown of outer layer similarity. Our research group recently performed channel flow simulations of acoustic liners [1] and found that outer layer similarity holds for the mean velocity, whereas it might break down for the Reynolds stresses.

Furthermore, the interaction of a turbulent flow with a permeable surface can change dramatically depending on the geometry, and unlike canonical (i.e homogeneous) permeable surfaces, acoustic liners have not been studied extensively. Experiments and numerical simulations of the flow over realistic liners are challenging. The diameter of the orifices d is significant with respect to the boundary layer thickness ($d/\delta \approx 0.1$) and much larger than the viscous length scale ($d^+ = d/\delta_v \approx 500$), where δ is the boundary layer thickness and $\delta_v = \nu_w/u_\tau$ is the viscous length scale based on $u_\tau = \sqrt{\tau_w/\rho_w}$ where ν_w, ρ_w and τ_w are the wall kinematic viscosity, wall density and the drag per plane area, respectively. Simultaneously satisfying these constraints on the diameter implies high computational cost. Therefore, previous numerical studies have avoided resolving the entire geometry. For instance, Scalo et al. [7] performed Large Eddy Simulation of turbulent channel flow with an impedance boundary condition modelling the liner. They performed simulations at a bulk Reynolds number of $Re_b = 6900$ and bulk Mach number of $M_b = 0.02$–0.5, and observed a drag increase of up to 350%.

Pore-resolved simulations of acoustic liners are scarce and typically employ simplifications to reduce the numerical cost [8, 9]. Zhang and Bodony [10] performed Direct Numerical Simulation (DNS) of a turbulent boundary layer over an acoustic liner cavity using the geometry studied at the Grazing Flow Impedance Tube (GFIT) facility at NASA [11]. However, Zhang and Bodony [10] simplified the geometry by studying a single cavity with a single orifice. Zhang and Bodony [10] performed DNS at $Re_\theta = 2300$ and Mach number $M = 0.5$, noting a drag increase of 4.2% without acoustic waves and 25% with $140dB$ acoustic waves. Our group has recently performed simulations of pore-resolved acoustic liner arrays [1, 12] where an array of cavities with multiple orifices within each cavity were studied. However, in order to be able to perform a parametric analysis, we opted for channel flow simulations to reduce computational cost and could not, therefore, capture how an acoustic liner would react to a changing boundary layer.

Our parametric analysis considered facesheets with different porosities and thicknesses, and quantified the drag increase of each surface. We noted that, in the absence of sound waves, facesheet permeability determines the acoustic liner behaviour and changes to the orifices that reduce the non-linear permeability should reduce the added drag. The added drag of several acoustic liner geometries has also been extensively documented through experiments at the GFIT [13–15]. These studies have helped identify geometrical parameters that can be fine-tuned to reduce acoustic liner drag. Howerton and Jones [13] note that reducing acoustic liner porosity while keeping the diameter constant reduces drag. Howerton and Jones [15] also identified novel geometries that could reduce drag while having similar acoustic performance. Therefore, there is significant room to aerodynamically optimise acoustic liners, which has largely been neglected until now, without compromising on acoustic performance.

Previous studies have attempted to characterise acoustic liner drag. However, most numerical studies applied simplifying models, such as the use of modelled boundary conditions and isolated cavities, and experiments are affected by significant uncertainties in the drag measurement and can not provide detailed information about turbulent flow structures. The discrepancies between previous studies are therefore very large. The present paper extends our recent

	σ	Re_τ	δ/δ_0	L_x/δ_0	N_x/δ_0	Δx^+_{min}	Δx^+_{max}	Δy^+_{min}	Δz^+_{min}	Δz^+_{max}
Smooth Region	0	854–1491	0.86–1.57	45	5824	4.26	8.26	0.79	4.26	4.46
Liner Region	0.322	1556–2587	1.58–2.43	70	15680	4.40	5.55	0.89	4.39	5.55

Table 1 DNS parameter for the smooth wall and acoustic liner sections of the domain. The wall-normal and spanwise extent of the domain is $L_y \times L_z = (15 + k)\delta_0 \times 5\delta_0$. The number of mesh points in the wall-normal and spanwise direction are $N_y \times N_z = 448 \times 1120$. σ is the porosity (open area ratio). Re_τ and δ/δ_0 show the variation of the friction Reynolds number and the bounday layer thickness in the domain. Δx^+, Δy^+ and Δz^+ are the viscous-scaled mesh spacing in the streamwise, wall-normal and spanwise direction.

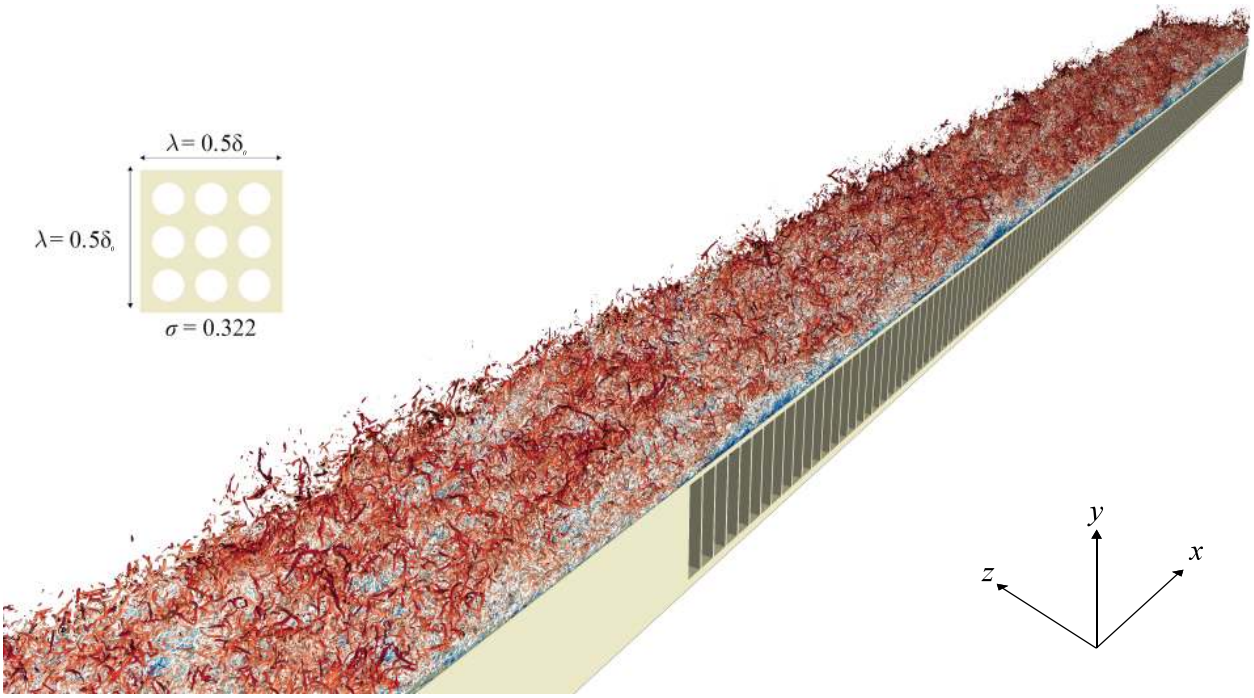

Fig. 1 Instantaneous flow field of the boundary layer simulation. Orifice configurations within a single cavity are also shown at the top left. Vortical structures are visualised using the Q-Criterion, coloured by the streamwise velocity.

work [1] on acoustic liners, by studying this surface in a more realistic numerical setup than ever done before, by performing DNS of turbulent boundary layer over fully resolved acoustic liner arrays.

III. Methodology

We perform DNS of a turbulent boundary layer over acoustic liners using the solver STREAmS [16, 17]. The simulation is performed in a rectangular box of size $L_x \times L_y \times L_z = 115\delta_0 \times (15 + k)\delta_0 \times 5\delta_0$, where δ_0 is the inflow boundary layer thickness, and k is the depth of the acoustic liner. Freestream Mach number is $M = u_\infty/c_\infty = 0.3$, where u_∞ is the freestream velocity and c_∞ is the speed of sound based on freestream conditions, and the friction Reynolds number is $Re_\tau \approx 800$–2400. The domain consists of an initial smooth wall region of length $L_{x,s} = 45\delta_0$, followed by an acoustic liner array that extends from $x/\delta_0 = 45$ to the end of the domain, $x/\delta_0 = 115$. The equations are discretized on a Cartesian grid with a mesh size $N_x \times N_y \times N_z = 21504 \times 448 \times 1120$. The mesh spacing is constant in the spanwise direction and points are clustered in the wall-normal direction at the liner facesheet and coarsened towards the backplate and the freestream. The mesh points in the streamwise direction are clustered close to the transition point between the smooth wall and the liner and then a constant mesh spacing is employed over the liner. Approximately 24 points are used in the streamwise and spanwise direction to resolve the orifice geometry. Details of the simulation are summarised in table 1. A non-reflecting boundary condition is employed at the outflow and top boundaries and a relaxation boundary condition is employed at the inflow [18]. Velocity fluctuations at the inflow are imposed using a recycling-rescaling procedure [19] and the recycling plane is located at $x/\delta_0 = 40$, $5\delta_0$ upstream of the point of transition from the smooth wall to the liner. Periodic boundary conditions are used in the spanwise direction. The geometry, consisting of the smooth wall and the liner, is resolved using a ghost-point immersed boundary method [20].

The geometry of the acoustic liners is chosen to match as closely as possible a realistic acoustic liner in operating conditions. Our cavity geometry has a square cross-section with a side length $\lambda = 0.5\delta_0$, depth, $k = 2.0\delta_0$. Each cavity has 9 orifices with diameter corresponding to a porosity of $\sigma = 0.322$. The geometry of the facesheet is similar to the one studied in our channel flow simulations [1] at $\sigma = 0.322$ and thickness to diameter ratio $t/d = 1$. The domain consists of a total of 140×10 acoustic liner cavities, with a total of 12600 orifices. An instantaneous flow visualisation of the flow field is shown in Figure 1 where vortices are visualised using the Q criterion. Top view of a single cavity

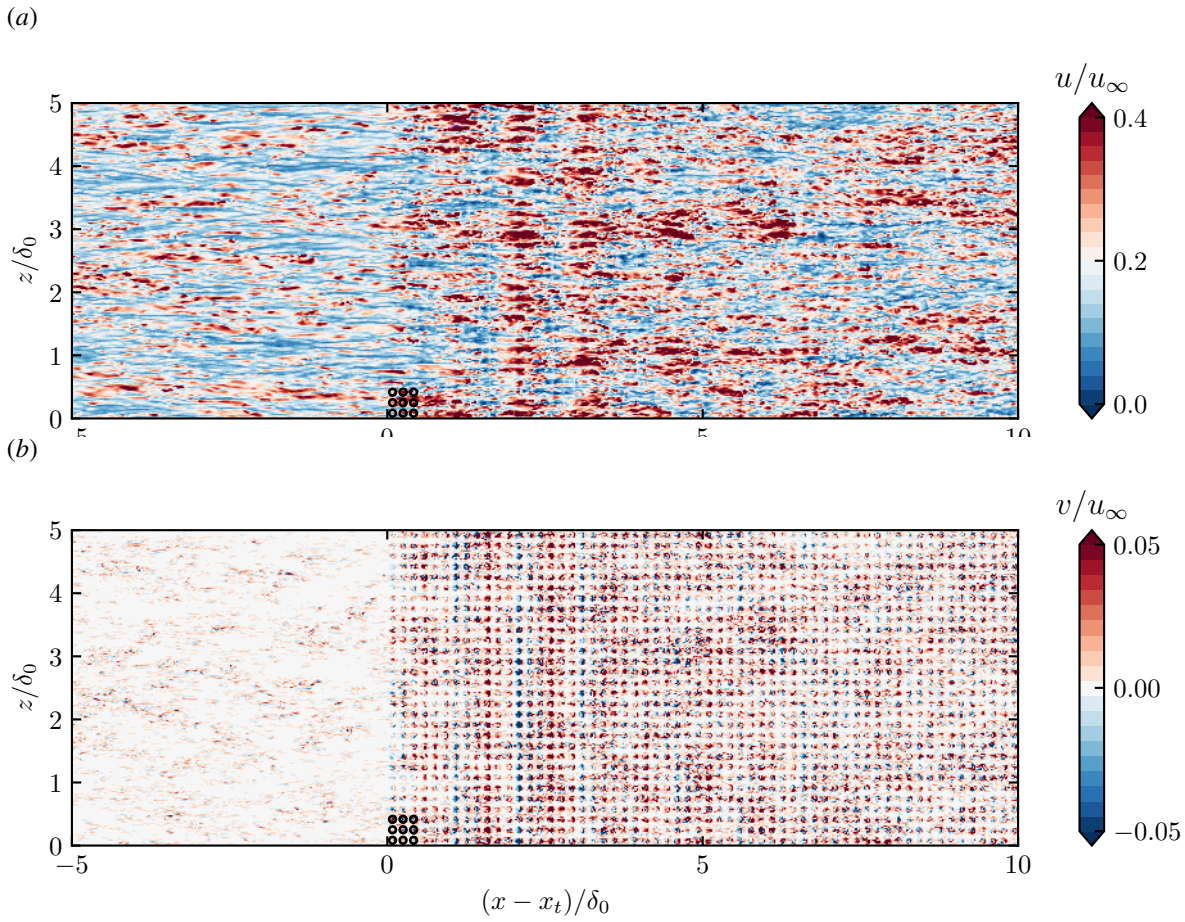

Fig. 2 Streamwise (*a*) and wall-normal (*b*) instantaneous velocity fluctuations in a wall parallel plane at $y^+ \approx 5$. The position of the orifices is shown for a single cavity at the smooth-to-rough transition. x_t represents the streamwise location of the smooth-to-rough transition point.

depicting the distribution of orifices is also shown in figure 1. The figure shows the complex organisation of the turbulent structures, and the growth of the boundary layer in the streamwise direction. Quantities that are non-dimensionalised by δ_v and u_τ are denoted by the '+' superscript.

IV. Results

A. Instantaneous flow field

Figure 2 shows the streamwise and wall-normal instantaneous velocity on an $x - z$ plane over the smooth-to-rough transition region. Compared to the smooth wall, the rough wall leads to very high wall-normal velocity near the surface of the facesheet, see figure 2 (*b*). High velocity magnitudes tend to be concentrated around the orifices, so much so that the position of the orifices is clearly visible in the velocity contours. Wall-normal velocity fluctuations have been previously observed to play an important role in altering the near wall cycle, for instance, by Kuwata and Suga [21], Endrikat et al. [22] and Orlandi and Leonardi [23], and have been proposed as the mechanism that leads to the drag increase over acoustic liners by Wilkinson [24] and Shahzad et al. [1]. Similar observations can be made for the streamwise velocity, see figure 2 (*a*). High-speed and low-speed streaks, typical of near-wall turbulence, are perturbed by the significant wall-normal velocity fluctuations at the wall and, thus, break down over the liner. Immediately after the smooth-to-rough transition, there exists a small region where we observe spanwise coherent structures that are probably the footprint of Kelvin-Helmholtz like structures, which disappear further downstream.

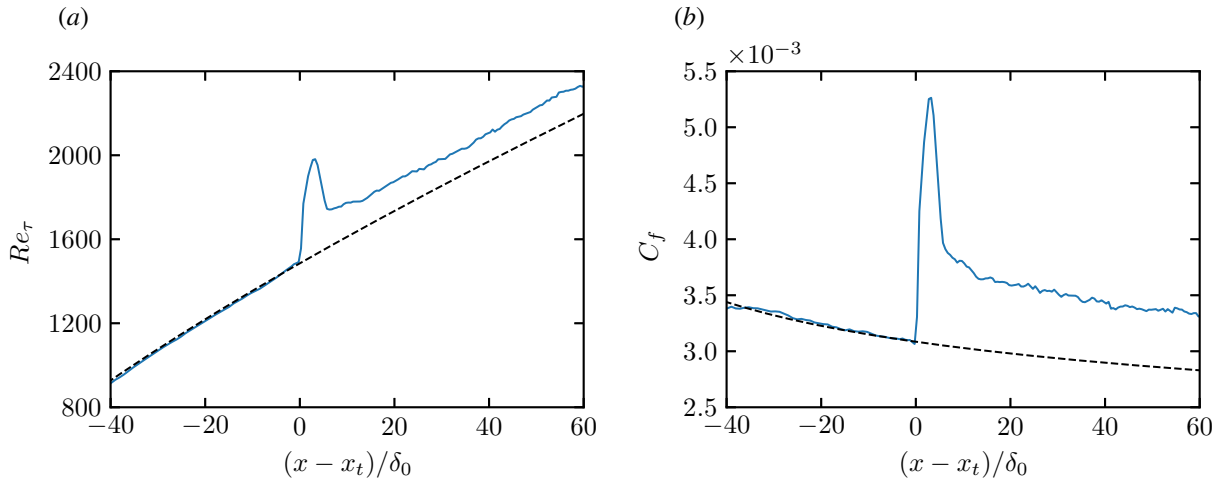

Fig. 3 Variation of the friction Reynolds number (*a*) and the skin-friction coefficient (*b*) for the boundary layer simulation with the distance from the smooth-to-rough transition point. Solid lines show the boundary layer simulation results and the dashed lines show smooth wall Re_τ and C_f for a smooth wall estimated using approximate turbulent boundary layer formulas.

B. Mean flow and skin-friction

The high wall-normal velocity fluctuations lead to an increase in drag over the acoustic liner. Figure 3 shows the friction Reynolds number, Re_τ, and the skin friction, C_f, as a function of the Reynolds number based on the momentum thickness. The region over the liner can largely be split into the smooth-to-rough transition region where rapid changes can be seen, and further downstream, where an almost self-similar behaviour is observed. Close to the point of transition, a sharp increase in the friction Reynolds number, evident in figure 3. Both the friction Reynolds number and the skin-friction coefficient tend to overshoot initially as the flow tries to adjust itself to the new flow conditions. Away from the transition location, the overshoot in the skin-friction coefficient decreases, but drag remains higher than for the smooth wall, as evidenced by the skin-friction coefficient in figure 3 (*b*).

Effects of the increase in drag can also be observed in the mean streamwise velocity over the liner, shown in figure 4 (*a*), where $\widetilde{\cdot}$ is the Favre averaging operator. Velocity profiles past the smooth-to-rough transition point show a downward shift as compared to the smooth wall. This downward shift, defined as $\Delta U^+ = \tilde{u}_s^+ - \tilde{u}_r^+$, where $\tilde{u}_s^+$ and $\tilde{u}_r^+$ are the streamwise velocities over the smooth wall and the acoustic liner in the logarithmic layer, respectively, is a measure of drag increase. Furthermore, the differences between the smooth wall velocity profile and that for the acoustic liner originate primarily near the wall and the velocity profiles are essentially parallel in the outer layer, indicating that Townsend's outer layer similarity hypothesis holds for the streamwise velocity. The streamwise velocity profiles over the rough wall exhibit essentially a constant ΔU^+, see figure 5 (*b*), apart from a small region near the smooth-to-rough transition point that exhibits higher skin friction.

Differences between the smooth and rough wall can also be seen in the Reynolds Stresses, $\tau_{ij} = \overline{\rho}\widetilde{u_i'' u_j''}$, shown in Figure 4 (*b*), where the double prime symbol indicates fluctuations with respect to the Favre average and $\overline{\cdot}$ is the Reynolds averaging operator. We compare the results of the liner simulations with the smooth-wall simulations of Eitel-Amor et al. [25] at approximately matching friction Reynolds number. Deviations from the smooth wall Reynolds stresses can be seen close to the wall. However, unlike the mean streamwise velocity, the Reynolds stresses deviate significantly even in the outer layer, indicating the possible breakdown of Townsend's outer layer similarity hypothesis for the velocity fluctuations. The peak streamwise Reynolds stress decreases over the acoustic liner and the peak spanwise and wall-normal velocity fluctuations increase with respect to the smooth wall, in contrast to the channel flow simulations of Shahzad et al. [1], for which we observed only an increase in the peak of the spanwise velocity fluctuations. The decrease in the peak of the streamwise velocity flucuations is due to the breakdown of the classical near-wall turbulence cycle due to the wall-normal velocity fluctuations. Irrespective of the velocity component, however, non-zero Reynolds stresses exist near the wall that enhance momentum transfer and contribute to the added drag. The non-zero wall-normal velocity fluctuations near the wall, also evident in the instantaneous flow in figure 2 (*b*), are what cause the breakdown of the classical near-wall turbulence cycle and a reduction in the streamwise Reynolds stress peak.

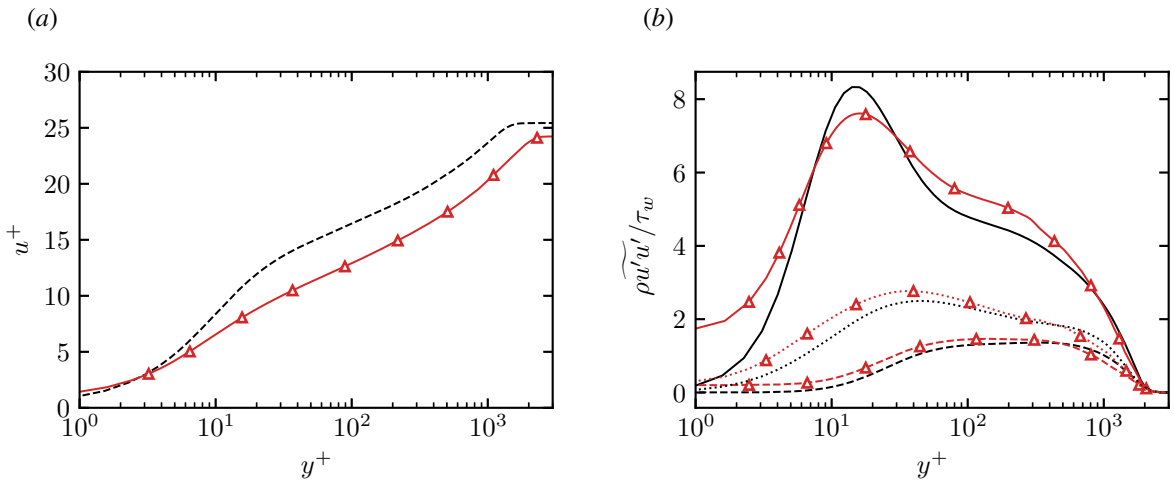

Fig. 4 Mean streamwise velocity (*a*) as a function of the wall-normal coordinate. Different line types represent different streamwise locations in panel (*a*): triangles ($(x - x_t)/\delta_0 \approx 45$) and dashed line ($(x - x_t)/\delta_0 \approx -5$). Streamwise (solid), wall-normal (dashed) and spanwise (dashed-dotted) Reynolds stresses (*b*) over the acoustic liner (symbols) compared to the smooth wall data of Eitel-Amor et al. [25] (without symbols) at friction Reynolds number, $Re_\tau \approx 1940$.

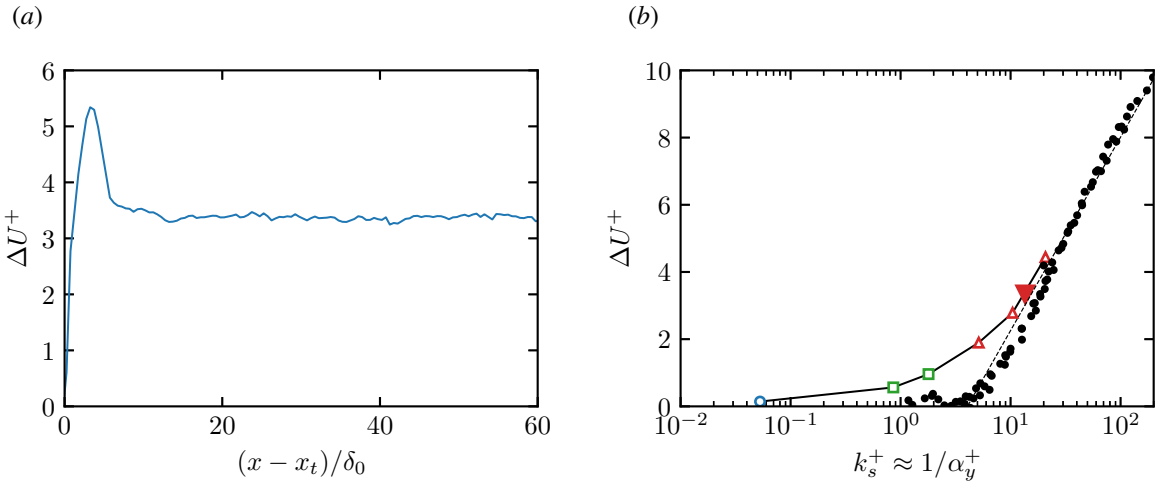

Fig. 5 ΔU^+ as a function of the distance from the transition point (*a*) and as a function of the viscous-scaled inverse of the Forchheimer coefficient (*b*). The filled inverted triangle represents ΔU^+ of the current simulation whereas the empty symbols represent data of channel flow simulations [1]. Filled circles are Nikuradse's data for sandgrain roughness.

C. Acoustic liners as a permeable substrate

Recently we have analysed several candidate length scales for acoustic liners [1] and observed that the inverse of the viscous-scaled non-linear permeability, $1/\alpha^+$, is the relevant length scale for acoustic liners. We attribute this to the very high inertial effects that may be observed inside the orifices. The present boundary layer results match quantitatively the results of our channel flow simulations [1]. Figure 5 (*b*) shows ΔU^+ as a function of the viscous-scaled inverse of the Forchheimer coefficient, which follows exactly the trend observed in the channel flow simulations. The good match is despite different cavity depth, $k/\delta = 0.822$–1.267 for our boundary layer simulation as compared to $k/\delta = 0.5$ for the channel flow simulations, where δ is the local boundary layer thickness and the channel half width, respectively. The cavity depth, therefore, does not play a significant role in determining liner behaviour in the absence of sound waves,.

Acoustic liner drag not being affected by cavity depth is in line with previous observations by Howerton and Jones [13], who noted that, in the absence of acoustic excitation, liner drag is not changed by changing the cavity depth. Therefore, the aerodynamics properties of acoustic liners are determined by the permeability of the facesheet and not by the cavity geometry.

V. Conclusion

We perform unprecedented DNS of a turbulent boundary layer over a fully resolved acoustic liner array in order to study the turbulent flow over these surfaces and understand their effect on the aerodynamic drag. Acoustic liners lead to an increase in drag and have a significant effect on the overlying turbulent flow. The present results for the Reynolds stresses suggests that the effect of the acoustic liners may extend to the outer layer, although this is not visible for the mean flow. Our boundary layer simulation, in conjunction with prior channel flow simulations, suggest that inertial effects dominate inside the perforations of the surface and it is the non-linear permeability that is the relevant parameter for this flow configuration instead of the Darcy permeability coefficient, which is typically used for canonical porous surfaces.

Acknowledgments

We acknowledge PRACE for awarding us access to Piz Daint, at the Swiss National Supercomputing Centre (CSCS), Switzerland.

References

[1] Shahzad, H., Hickel, S., and Modesti, D., "Turbulence and added drag over acoustic liners," *arXiv:2210.17354 [physics]*, 2022. https://doi.org/10.48550/arXiv.2210.17354.

[2] Sivian, L. J., "Acoustic impedance of small orifices," *J. Acoust. Soc*, Vol. 7, No. 2, 1935, pp. 94–101. https://doi.org/10.1121/1.1915795.

[3] Ingård, U., and Labate, S., "Acoustic circulation effects and the nonlinear impedance of orifices," *J. Acoust. Soc. Am.*, Vol. 22, No. 2, 1950, pp. 211–218. https://doi.org/10.1121/1.1906591.

[4] Manes, C., Pokrajac, D., McEwan, I., and Nikora, V., "Turbulence structure of open channel flows over permeable and impermeable beds: A comparative study," *Phys. Fluids*, Vol. 21, No. 12, 2009, p. 125109. https://doi.org/10.1063/1.3276292.

[5] Breugem, W. P., Boersma, B. J., and Uittenbogaard, R. E., "The influence of wall permeability on turbulent channel flow," *J. Fluid Mech.*, Vol. 562, 2006, pp. 35–72. https://doi.org/10.1017/S0022112006000887.

[6] Kuwata, Y., and Suga, K., "Direct numerical simulation of turbulence over anisotropic porous media," *J. Fluid Mech.*, Vol. 831, 2017, pp. 41–71. https://doi.org/10.1017/jfm.2017.619.

[7] Scalo, C., Bodart, J., and Lele, S. K., "Compressible turbulent channel flow with impedance boundary conditions," *Phys. Fluids*, Vol. 27, No. 3, 2015, p. 035107. https://doi.org/10.1063/1.4914099.

[8] Tam, C. K. W., Ju, H., Jones, M. G., Watson, W. R., and Parrott, T. L., "A computational and experimental study of resonators in three dimensions," *J. Sound Vib.*, Vol. 329, No. 24, 2010, pp. 5164–5193. https://doi.org/10.1016/j.jsv.2010.06.005.

[9] Avallone, F., Manjunath, P., Ragni, D., and Casalino, D., "Lattice-Boltzmann Very Large Eddy Simulation of a Multi-Orifice Acoustic Liner with Turbulent Grazing Flow," *AIAA paper 2019-2542*, 2019. https://doi.org/10.2514/6.2019-2542.

[10] Zhang, Q., and Bodony, D. J., "Numerical investigation of a honeycomb liner grazed by laminar and turbulent boundary layers," *J. Fluid Mech.*, Vol. 792, 2016, pp. 936–980. https://doi.org/10.1017/jfm.2016.79.

[11] Jones, M., Watson, W. R., Parrott, T., and Smith, C., "Design and evaluation of modifications to the NASA Langley flow impedance tube," *AIAA paper 2004-2837*, 2004. https://doi.org/10.2514/6.2004-2837.

[12] Shahzad, H., Hickel, S., and Modesti, D., "Permeability and turbulence over perforated plates," *Flow. Turbul. Combust.*, Vol. 109, No. 4, 2022, p. 1241–1254. https://doi.org/10.1007/s10494-022-00337-7.

[13] Howerton, B. M., and Jones, M. G., "Acoustic liner drag: a parametric study of conventional configurations," *AIAA paper 2015-2230*, 2015. https://doi.org/10.2514/6.2015-2230.

[14] Howerton, B. M., and Jones, M. G., "Acoustic liner drag: measurements on novel facesheet perforate geometries," *AIAA paper 2016-2979*, 2016. https://doi.org/10.2514/6.2016-2979.

[15] Howerton, B. M., and Jones, M. G., "A conventional liner acoustic/drag interaction benchmark database," *AIAA paper 2017-4190*, 2017. https://doi.org/10.2514/6.2017-4190.

[16] Bernardini, M., Modesti, D., Salvadore, F., Sathyanarayana, S., Della Posta, G., and Pirozzoli, S., "STREAmS-2.0: Supersonic turbulent accelerated Navier-Stokes solver version 2.0," *Computer Physics Communications*, Vol. 285, 2023, p. 108644. https://doi.org/10.1016/j.cpc.2022.108644.

[17] Sathyanarayana, S., Bernardini, M., Modesti, D., Pirozzoli, S., and Salvadore, F., "High-speed turbulent flows towards the exascale: STREAmS-2 porting and performance," *arXiv:2304.05494 [physics]*, 2023. https://doi.org/10.48550/arXiv.2304.05494.

[18] Pirozzoli, S., and Colonius, T., "Generalized characteristic relaxation boundary conditions for unsteady compressible flow simulations," *Journal of Computational Physics*, Vol. 248, 2013, pp. 109–126. https://doi.org/10.1016/j.jcp.2013.04.021, URL https://linkinghub.elsevier.com/retrieve/pii/S0021999113002866.

[19] Pirozzoli, S., Bernardini, M., and Grasso, F., "Direct numerical simulation of transonic shock/boundary layer interaction under conditions of incipient separation," *J. Fluid Mech.*, Vol. 657, 2010, pp. 361–393. https://doi.org/10.1017/S0022112010001710.

[20] Vanna, F. D., Picano, F., and Benini, E., "A sharp-interface immersed boundary method for moving objects in compressible viscous flows," *Comput. Fluids*, Vol. 201, 2020, p. 104415. https://doi.org/10.1016/j.compfluid.2019.104415.

[21] Kuwata, Y., and Suga, K., "Lattice Boltzmann direct numerical simulation of interface turbulence over porous and rough walls," *Int. J. Heat Fluid Flow*, Vol. 61, 2016, pp. 145–157. https://doi.org/10.1016/j.ijheatfluidflow.2016.03.006.

[22] Endrikat, S., Modesti, D., García-Mayoral, R., Hutchins, N., and Chung, D., "Influence of riblet shapes on the occurrence of Kelvin–Helmholtz rollers," *J. Fluid Mech.*, Vol. 913, 2021. https://doi.org/10.1017/jfm.2021.2.

[23] Orlandi, P., and Leonardi, S., "DNS of turbulent channel flows with two- and three-dimensional roughness," *J. Turbul.*, Vol. 7, 2006, p. N73. https://doi.org/10.1080/14685240600827526.

[24] Wilkinson, S., "Influence of wall permeability on turbulent boundary-layer properties," *AIAA paper 1983-294*, Reno,NV,U.S.A., 1983. https://doi.org/10.2514/6.1983-294.

[25] Eitel-Amor, G., Örlü, R., and Schlatter, P., "Simulation and validation of a spatially evolving turbulent boundary layer up to Re_θ=8300," *Int. J. Heat Fluid Flow*, Vol. 47, 2014, pp. 57–69. https://doi.org/10.1016/j.ijheatfluidflow.2014.02.006.